# Spin-splitting in electric-potential-difference antiferromagnetism

San-Dong Guo

School of Electronic Engineering, Xi'an University of Posts and Telecommunications, Xi'an 710121, China

The antiferromagnetic (AFM) materials are robust to external magnetic perturbation due to missing any net magnetic moment. In general, the spin splitting in the band structures disappears in these antiferromagnets. However, the altermagnetism can achieve spin-split bands in collinear symmetry-compensated antiferromagnet with special magnetic space group. Here, we propose a new mechanism that can achieve spin splitting in two-dimensional (2D) Janus A-type AFM materials. Since the built-in electric field caused by Janus structure creates a layer-dependent electrostatic potential, the electronic bands in different layers will stagger, producing the spin splitting, which can be called electric-potential-difference antiferromagnetism (EPD-AFM). We demonstrate that Janus monolayer Mn<sub>2</sub>ClF is a possible candidate to achieve the EPD-AFM by the first-principles calculations. It is proposed that the spin splitting can be tuned in EPD-AFM by piezoelectric effect. Our works provide a new design principle for generating spin polarization in 2D AFM materials.

Keywords: Spin-split bands, Antiferromagnetism, Built-in electric field Email:sandongyuwang@163.com

### I. INTRODUCTION

The spin splitting in the band structures can be produced by utilizing the effect of spin-orbit coupling  $(SOC)^1$ . A general form of the SOC Hamiltonian  $H_{SOC}$  in solid-state materials with a lack of inversion symmetry can be expressed as<sup>2,3</sup>:

$$H_{SOC} = \vec{\Omega}(\vec{k}) \cdot \vec{\sigma} = \alpha(\vec{E} \times \vec{k}) \cdot \vec{\sigma} \tag{1}$$

Where the  $\vec{\Omega}(\vec{k})$  is known as a spin-orbit field (SOF) as an effective magnetic field,  $\alpha$  is the strength of the SOC,  $\vec{E}$  is the local electric field induced by the crystal inversion asymmetry,  $\vec{k}$  is is the wave vector, and  $\vec{\sigma} = (\sigma_x, \sigma_y, \sigma_z)$  are the Pauli matrices.

If a two-dimensional (2D) material possesses out-ofplane built-in electric field, Equation 1 will become:

$$H_{SOC} = \alpha_R (k_x \sigma_y - k_y \sigma_x) \tag{2}$$

This is known as Rashba SOC Hamiltonian<sup>4</sup>, and  $\alpha_R$  is the so-called Rashba parameter. Here, the spin S only has the in-plane components  $S_x$  and  $S_y$ , which depend on the momentum of electrons. The impurities and defects can change the momentum of electrons, which can randomize the spin due to the k-dependent SOF, and then induce spin decoherence through the Dyakonov-Perel (DP) mechanism<sup>5</sup>.

If a 2D material possesses in-plane built-in electric field, for example along x direction, Equation 1 will be reduced into:

$$H_{SOC} = \alpha_D k_y \sigma_z \tag{3}$$

Here, the spin S only has the out-of-plane component  $S_z$ . The SOF orientation of Equation 3 is unidirectional, which will lead to a spatially periodic mode of the spin polarization, known as the persistent spin helix (PSH)<sup>6,7</sup>. The PSH can suppress spin dephasing due to SU(2) spin rotation symmetry, producing an extremely long spin lifetime<sup>6,8</sup>.

The spin splitting can also be observed in ferromagnetic (FM) materials. Superior to FM materials, the antiferromagnetic (AFM) materials are robust to external magnetic perturbation due to missing any net magnetic moment, which allows high-speed device operation  $^{9,10}$ . In general, the spin splitting in the band structures is lacking in these antiferromagnets. However, the spin splitting has been realized in collinear symmetry-compensated antiferromagnet, and the SOC is not needed, which is called altermagnetism  $^{11-13}$ . Several 2D materials have been predicted to be altermagnetic materials, such as  $\mathrm{Cr}_2\mathrm{O}_2^{14,15}$ ,  $\mathrm{Cr}_2\mathrm{SO}^{16}$  and  $\mathrm{V}_2\mathrm{Se}_2\mathrm{O}^{17}$ .

Here, we propose a new mechanism to achieve spin splitting in AFM materials. For a 2D material, the magnetic atoms have opposite layer spin polarization, namely A-type AFM ordering. If the out-of-plane built-in electric field is lacking, the degeneration of electron spin in the band structures is observed (Figure 1 (a) and (b)). For a 2D Janus material, the magnetic configuration is still A-type AFM ordering, but it has an out-of-plane builtin electric field  $E_b$ , which will destroy the degeneration of electron spin in the band structures (Figure 1 (c) and (d)). This is because the built-in electric field creates a layer-dependent electrostatic potential, and the electronic bands in different layers will stagger, which gives rise to the spin splitting. The spin splitting in 2D Janus A-type AFM materials can be called electric-potentialdifference antiferromagnetism (EPD-AFM).

Recently, the electric-field control of spin polarization in 2D A-type AFM semiconductor  $\rm Mn_2Cl_2$  has been reported, and the 100% spin polarization via electric field can be achieved Based on  $\rm Mn_2Cl_2$ , Janus monolayer  $\rm Mn_2ClF$  is constructed by replacing one of two Cl layers with F atoms, which is proved to be a possible candidate to achieve the EPD-AFM by the first-principles calculations. Calculated results show that EPD-AFM in  $\rm Mn_2ClF$  is robust against the electronic correlation. The piezoelectric properties of  $\rm Mn_2ClF$  are also investigated, and the out-of-plane piezoelectric response may be used to tune the spin splitting. These findings enrich the types

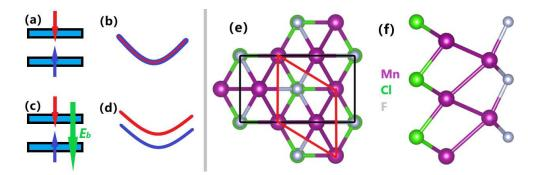


FIG. 1. (Color online) (a): for a 2D material, the magnetic atoms have opposite layer spin polarization (A-type antiferromagnetic ordering) without the out-of-plane built-in electric field, producing the degeneration of electron spin (b); (c): for a 2D Janus material, the magnetic atoms have opposite layer spin polarization (A-type antiferromagnetic ordering) with the out-of-plane built-in electric field  $E_b$ , destroying the degeneration of electron spin (d). (e) and (f): for Janus monolayer Mn<sub>2</sub>ClF, the top and side views of the crystal structures. In (a), the rhombus primitive cell (rectangle supercell) is marked by the red (black) frame.

of spin splitting, which is useful for spintronic device applications.

### II. COMPUTATIONAL DETAIL

Within density functional theory (DFT)<sup>19</sup>, the spin-polarized first-principles calculations are carried out within the projector augmented-wave (PAW) method by using the standard VASP code<sup>20–22</sup>. We use the generalized gradient approximation of Perdew-Burke-Ernzerhof (PBE-GGA)<sup>23</sup> as the exchange-correlation functional. To account for electron correlation of Mn-3d orbitals, we use a Hubbard correction  $U_{eff}$ =4.00 eV<sup>24–26</sup> within the rotationally invariant approach proposed by Dudarev et al. The kinetic energy cutoff of 500 eV, total energy convergence criterion of 10<sup>-8</sup> eV, and force convergence criterion of 0.0001 eV.Å<sup>-1</sup> are set to obtain the accurate results. A vacuum of more than 16 Å is used to avoid out-of-plane interaction.

The elastic stiffness tensor  $C_{ij}$  and piezoelectric stress tensor  $e_{ij}$  are calculated by using strain-stress relationship (SSR) method and density functional perturbation theory (DFPT) method<sup>27</sup>, respectively. The  $C_{ij}^{2D}/e_{ij}^{2D}$  has been renormalized by  $C_{ij}^{2D}=L_zC_{ij}^{3D}/e_{ij}^{2D}=L_ze_{ij}^{3D}$ , where the  $L_z$  is the length of unit cell along z direction. We use a  $21\times21\times1$  k-point meshes to sample the Brillouin zone (BZ) for calculating electronic structures and elastic properties, and a  $10\times21\times1$  k-point meshes for piezoelectric calculations. The interatomic force constants (IFCs) are calculated by using a  $5\times5\times1$  supercell within finite displacement method, and the phonon dispersion spectrum can be calculated by the Phonopy code<sup>28</sup>. The elastic, piezoelectric, phonon and ab-initio molecular dynamics (AIMD) calculations are all performed with AFM1 magnetic configuration.

### III. CRYSTAL STRUCTURE AND STABILITY

Monolayer  $Mn_2ClF$  possesses similar crystal structures with  $Mn_2Cl_2^{18}$ , consisting of four atomic layers in the sequence of Cl-Mn-Mn-F (see Figure 1 (e) and (f)). It is clearly seen that the magnetic Mn atoms distribute in two layers, and an intrinsic polar electric field along the out-of-plane direction can be induced due to the different electronegativity of the Cl and F elements, which provides possibility to realize EPD-AFM. The Janus monolayer  $Mn_2ClF$  can be constructed by replacing one of two Cl layers with F atoms in monolayer  $Mn_2Cl_2$ . The  $Mn_2Cl_2$  possesses  $P\bar{3}m1$  space group (No.164), and the space group of  $Mn_2ClF$  is reduced into P3m1 (No.156) due to broken horizontal mirror symmetry, which will produce both in-plane and out-of-plane piezoelectricity.

To determine magnetic ground state of Mn<sub>2</sub>ClF, the rectangle supercell (see Figure 1 (e)) is used to construct FM and three AFM configurations (AFM1, AFM2) and AFM3). These magnetic configurations are shown in FIG.1 of electronic supplementary information (ESI), and the AFM1 is called A-type AFM state. Calculated results show that the AFM1 configuration is ground state of Mn<sub>2</sub>ClF, and its energy per unit cell is 0.43 eV, 0.32 eV and 0.23 eV lower than those of FM, AFM2 and AFM3 cases by GGA+U. The optimized lattice constants a=b=3.43 Å by GGA+U for AFM1 case. The magnetic easy-axis is confirmed by magnetic anisotropy energy (MAE), which is defined as the energy difference of the magnetization orientation along the (100) and (001) cases within SOC. The Calculated MAE is only 1  $\mu eV/Mn$ , which indicates that the easy-axis of Mn<sub>2</sub>ClF is out-of-plane.

To validate the dynamic, thermal and mechanical stabilities of Mn<sub>2</sub>ClF, the phonon spectra, AIMD and elastic constants are calculated, respectively. The calculated phonon spectrum of Mn<sub>2</sub>ClF with no obvious imaginary frequencies is plotted in FIG.2 of ESI, indicating its dynamic stability. The AIMD simulations using NVT en-

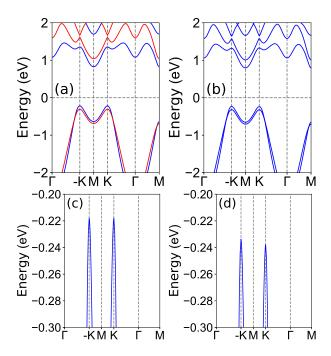


FIG. 2. (Color online)For Mn<sub>2</sub>ClF, the energy band structures without SOC (a) and with SOC (b). In (a), the spin-up and spin-down channels are depicted in blue and red. The (c) and (d) are the partial enlarged drawing of (a) and (b) near the Fermi level for the valence bands.

semble are carried out for more than 8000 fs with a time step of 1 fs by using a  $4\times4\times1$  supercell at 300 K. According to FIG.3 of ESI, during the simulation, the crystal structures of Mn<sub>2</sub>ClF are maintained without structural fracture, and the energies are kept stable, confirming its thermal stability. Two independent elastic constants  $C_{11}$  and  $C_{12}$  of Mn<sub>2</sub>ClF are 56.66 Nm<sup>-1</sup> and 17.22 Nm<sup>-1</sup>, which satisfy the Born criteria of mechanical stability:  $C_{11} > 0$  and  $C_{11} - C_{12} > 0^{29}$ , confirming its mechanical stability.

## IV. ELECTRONIC STRUCTURES

The magnetic moments of bottom and top Mn atoms are  $4.57~\mu_B$  and  $-4.52~\mu_B$ , and total magnetic moment per unit cell is strictly  $0.00~\mu_B$ . In general, no spin splitting can be observed for AFM material. However, our proposed Mn<sub>2</sub>ClF shows obvious spin splitting from calculated energy band structures without SOC in Figure 2 (a). This is very different from energy band structures of Mn<sub>2</sub>Cl<sub>2</sub> (see FIG.4 of ESI), where no spin splitting exists. This difference is because the Mn<sub>2</sub>ClF possesses the out-of-plane polar electric field, while the built-in electric field of Mn<sub>2</sub>Cl<sub>2</sub> disappears. It is clearly seen that Mn<sub>2</sub>ClF is an indirect band gap semiconductor with gap value of 1.043 eV. The valence band maximum (VBM) and conduction band bottom (CBM) are at high symmetry K/-K and M points, respectively, and they are pro-

vided by the same spin-up channel. When including the SOC, the energy band structures of Mn<sub>2</sub>ClF have very small changes, and it is still an indirect bandgap semiconductor with reduced gap value of 1.028 eV (Figure 2 (b)). Without considering SOC, the K and -K valleys of valence bands are exactly degenerate (Figure 2 (c)). However, when SOC is switched on, the energy degeneracy between the K and - K valleys is lifted due to broken space- and time-inversion symmetries, leading to an interesting phenomenon of the spontaneous valley polarization with very small valley splitting of 4.3 meV (Figure 2) (d)). This is different from the common valley splitting in FM materials<sup>30</sup>. Recently, the spontaneous valley polarization is also predicted in 2D AFM Mn<sub>2</sub>P<sub>2</sub>S<sub>3</sub>Se<sub>3</sub> with a valley splitting of 16.3 meV<sup>31</sup>. For Mn<sub>2</sub>ClF, the layercharacters energy band structures without SOC and with SOC are plotted in Figure 3. Calculated results show that the weights of spin-up and spin-down of both valence and conduction bands are reversed in different Mn layers (Figure 3 (a) and (b)), which gives rise to the obvious spin splitting. According to Figure 3 (c), it is clearly seen that two Mn layers are non-equivalent due to a layerdependent electrostatic potential caused by the built-in electric field.

The electronic correlation can produce important effects on the magnetic ground state, electronic structures and topological properties of 2D magnetic materials<sup>32–36</sup>. To confirm robust EPD-AFM, the electronic correlation effects on physical properties of Mn<sub>2</sub>ClF are considered by using different U values. Firstly, the lattice constants a of Mn<sub>2</sub>ClF are optimized by GGA+U (0-5 eV), and then calculate its related physical properties. Based on FIG.5 of ESI, the lattice constants a (3.286 Å-3.447  $\dot{A}$ ) increases with increasing U. To achieve EPD-AFM, the AFM1 magnetic configuration as the ground state of Mn<sub>2</sub>ClF is a crucial factor. So, the energy differences between FM/AFM2/AFM3 and AFM1 (per unit cell) as a function of U are plotted in Figure 4. It is found that Mn<sub>2</sub>ClF is always a AFM1 ground state in considered U range. The evolutions of energy band structures as a function of U are plotted in Figure 5, and the total gap vs U is shown in FIG.6 of ESI. In considered U range, the Mn<sub>2</sub>ClF is always an indirect gap semiconductor, and shows obvious spin splitting. The VBM and CBM are always at high symmetry K/-K and M points, which are provided by the same spin-up channel. Finally, the MAE as a function of U is plotted in FIG.7 of ESI. When U is less than about 4.7 eV, the out-of-plane magnetic anisotropy can be maintained. These results show that the EPD-AFM of Mn<sub>2</sub>ClF is robust.

### V. PIEZOELECTRIC PROPERTIES

The Mn<sub>2</sub>Cl<sub>2</sub> monolayer possesses no piezoelectricity because of inversion symmetry. However, due to broken horizontal mirror symmetry, the monolayer Mn<sub>2</sub>ClF has both in-plane and out-of-plane piezoelectricity. The

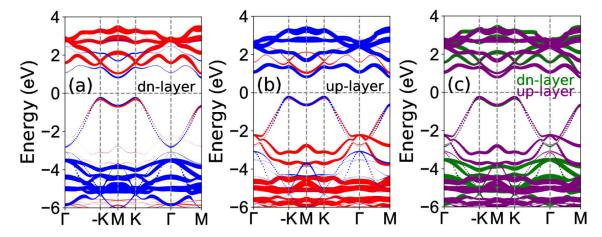


FIG. 3. (Color online)For  $Mn_2ClF$ , the layer-characters energy band structures without SOC (a and b) and with SOC (c). In (a) and (b), the spin-up and spin-down channels are depicted in blue and red. The (a) means dn-layer-characters energy band structures, while the (b) shows up-layer-characters energy band structures. In (c), the spin-up and spin-down channels are not distinguished.

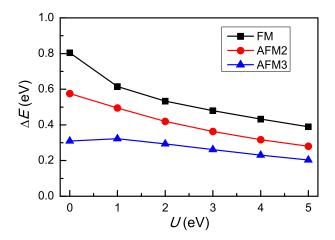


FIG. 4. (Color online)For  $Mn_2ClF$ , the energy differences between FM/AFM2/AFM3 and AFM1 (per unit cell) as a function of U.

piezoelectric response of a material can be described by the third-rank piezoelectric stress tensor  $e_{ijk}$  and strain tensor  $d_{ijk}$ , which can be expressed as the sum of ionic and electronic contributions:

$$e_{ijk} = \frac{\partial P_i}{\partial \varepsilon_{jk}} = e_{ijk}^{elc} + e_{ijk}^{ion}$$

$$d_{ijk} = \frac{\partial P_i}{\partial \sigma_{jk}} = d_{ijk}^{elc} + d_{ijk}^{ion}$$
(4)

In which  $P_i$ ,  $\varepsilon_{jk}$  and  $\sigma_{jk}$  are polarization vector, strain and stress, respectively. The superscripts elc/ion means electronic/ionic contribution. The  $e^{elc}_{ijk}$  and  $d^{elc}_{ijk}$  are called clamped-ion piezoelectric coefficients, while the  $e_{ijk}$  and  $d_{ijk}$  are called relaxed-ion piezoelectric coefficients. The  $e_{ijk}$  is related with  $d_{ijk}$  by elastic tensor  $C_{mnjk}$ :

$$e_{ijk} = \frac{\partial P_i}{\partial \varepsilon_{jk}} = \frac{\partial P_i}{\partial \sigma_{mn}} \cdot \frac{\partial \sigma_{mn}}{\partial \varepsilon_{jk}} = d_{imn} C_{mnjk}$$
 (5)

By using Voigt notation, when only considering the inplane strain and stress<sup>37–39</sup>, the Equation 5 with P3m1 symmetry can be reduced into:

$$\begin{pmatrix} e_{11} & -e_{11} & 0 \\ 0 & 0 & -e_{11} \\ e_{31} & e_{31} & 0 \end{pmatrix} = \begin{pmatrix} d_{11} & -d_{11} & 0 \\ 0 & 0 & -2d_{11} \\ d_{31} & d_{31} & 0 \end{pmatrix}$$

$$\begin{pmatrix} C_{11} & C_{12} & 0 \\ C_{12} & C_{11} & 0 \\ 0 & 0 & (C_{11} - C_{12})/2 \end{pmatrix}$$
(6)

With an imposed uniaxial in-plane strain, both in-plane and out-of-plane piezoelectric polarization can be produced  $(e_{11}/d_{11}\neq 0)$  and  $e_{31}/d_{31}\neq 0)$ . However, when a biaxial in-plane strain is applied, the in-plane component will disappear  $(e_{11}/d_{11}=0)$ , but the out-of-plane component still exists  $(e_{31}/d_{31}\neq 0)$ . By solving the Equation 6, the two independent  $d_{11}$  and  $d_{31}$  can be derived:

$$d_{11} = \frac{e_{11}}{C_{11} - C_{12}} \quad and \quad d_{31} = \frac{e_{31}}{C_{11} + C_{12}} \tag{7}$$

The orthorhombic supercell (see Figure 1 (e)) as the computational unit cell is used to calculate the  $e_{11}/e_{31}$  of  $\mathrm{Mn_2ClF}$ . The calculated  $e_{11}/e_{31}$  is  $-0.745\times10^{-10}/-0.191\times10^{-10}$  C/m with ionic part  $-0.647\times10^{-10}/0.372\times10^{-10}$  C/m and electronic part  $-0.098\times10^{-10}/-0.563\times10^{-10}$  C/m. For  $e_{11}$ , the same signs can be observed for the electronic and ionic contributions, and the ionic part plays a decisive role. However, for  $e_{31}$ , the electronic and ionic contributions have opposite signs, and the electronic part dominates the piezoelectricity. Based on Equation 7, the calculated  $d_{11}$  and  $d_{31}$  of  $\mathrm{Mn_2ClF}$  are -1.89 and -0.26 pm/V, respectively. The predicted  $|d_{31}|$  is higher than or compared with those of other 2D known materials  $^{37-39}$ , which provides possibility to tune spin splitting in  $\mathrm{Mn_2ClF}$  by piezoelectric effect.

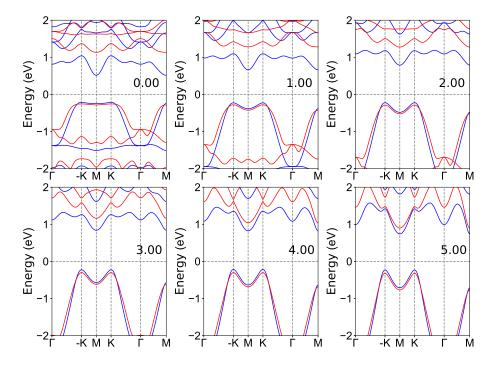


FIG. 5. (Color online) The energy band structures of  $Mn_2ClF$  at representative U without SOC. The spin-up and spin-down channels are depicted in blue and red.

Electric-field induced spin splitting in  $\rm Mn_2Cl_2$  has been confirmed by the first-principles calculations<sup>18</sup>. The out-of-plane electric field can tune the spin splitting in  $\rm Mn_2ClF$ . When a biaxial in-plane strain is imposed, only out-of-plane  $d_{31}$  appears, and an out-of-plane electric field can be induced, which can be used to tune spin splitting in  $\rm Mn_2ClF$ . Piezotronic effect on Rashba spin splitting in a  $\rm ZnO/P3HT$  nanowire array structure has been studied experimentally<sup>40</sup>. It is found that the Rashba spin splitting can be effectively tuned by innercrystal piezo-potential created inside the  $\rm ZnO$  nanowires. So, the coupling between spin splitting and piezoelectric effect may be observed by  $\rm EPD\text{-}AFM$ .

#### VI. DISCUSSION AND CONCLUSION

For a 2D altermagnet, the magnetic atoms have opposite layer spin polarization (A-type AFM ordering). If the out-of-plane built-in electric field is lacking, the obvious spin splitting in the band structures can still be observed (Figure 6 (a) and (b)). However, the spin-valley polarization is lacking. Recently, this have been achieved in 2D  $Ca(CoN)_2^{41}$ . For a 2D Janus altermagnet, the magnetic configuration is still A-type AFM ordering, but it has an out-of-plane built-in electric field  $E_b$ , which will produce spin-valley polarization(Figure 6 (c) and (d)). This is because a layer-dependent electrostatic potential makes electronic bands in different layers stagger, producing the spin-valley polarization. The out-of-plane polarization filed is equivalent to an external electric field<sup>42</sup>. By ap-

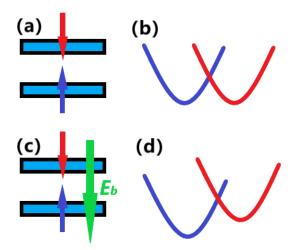


FIG. 6. (Color online)(a): for a 2D altermagnet, the magnetic atoms have opposite layer spin polarization (A-type antiferromagnetic ordering) without the out-of-plane built-in electric field, destroying the degeneration of electron spin without spin-valley polarization (b); (c): for a 2D Janus altermagnet, the magnetic atoms have opposite layer spin polarization (A-type antiferromagnetic ordering) with the out-of-plane built-in electric field  $E_b$ , destroying the degeneration of electron spin with spin-valley polarization (d).

plying a gate field of  $0.2 \, \mathrm{eV/\AA}$ , monolayer  $\mathrm{Ca(CoN)_2}$  possesses a significant spin-valley splitting up to  $123 \, \mathrm{meV^{41}}$ . So, an out-of-plane built-in electric field can induce spin-valley polarization. The 2D Janus A-type altermagnetic material can be called electric-potential-difference alter-

### magnet (EPD-AM).

In summary, we propose an alternative strategy to obtain spin splitting based on 2D Janus A-type antiferromagnet. It is demonstrated that 2D  $\rm Mn_2ClF$  is a possible candidate for realizing EPD-AFM, which is dynamically, mechanically and thermally stable. It is proved that the EPD-AFM is robust against electron correlation in  $\rm Mn_2ClF$ . The structural symmetry-breaking leads to out-of-plane piezoelectric response, providing a possibility to tune spin splitting in  $\rm Mn_2ClF$  by piezoelectric effect. Our works reveal a new 2D family of AFM materials with spin splitting, which allow high-speed spintronic device applications.

## ACKNOWLEDGMENTS

This work is supported by Natural Science Basis Research Plan in Shaanxi Province of China (2021JM-456). We are grateful to the China University of Mining and Technology (CUMT) for VASP software to accomplish this work. We are grateful to Shanxi Supercomputing Center of China, and the calculations were performed on TianHe-2.

- J. Nitta, T. Akazaki, H. Takayanagi, and T. Enoki, Phys. Rev. Lett. 78, 1335 (1997).
- <sup>2</sup> J. Nitta, T. Akazaki, H. Takayanagi and T. Enoki, Phys. Rev. Lett. 78, 1335 (1997).
- <sup>3</sup> A. Manchon, H. C. Koo, J. Nitta, S. M. Frolov and R. A. Duine, Nat. Mater. **14**, 871 (2015).
- <sup>4</sup> E. I. Rashba, Sov. Phys. Solid State **2**, 1224 (1960).
- M. I. Dyakonov and V. I. Perel, Sov. Phys. Solid State 13, 3023 (1972).
- <sup>6</sup> B. A. Bernevig, J. Orenstein, and S.-C. Zhang, Phys. Rev. Lett. **97**, 236601 (2006).
- <sup>7</sup> J. Schliemann, Rev. Mod. Phys. 89, 011001 (2017).
- <sup>8</sup> P. Altmann, M. P. Walser, C. Reichl, W. Wegscheider, and G. Salis, Phys. Rev. B **90**, 201306(R) (2014).
- <sup>9</sup> X. Hu, Adv. Mater. **24**, 294 (2012).
- <sup>10</sup> T. Jungwirth, J. Sinova, A. Manchon, X. Marti, J. Wunderlich and C. Felser, Nat. Phys. 14, 200 (2018).
- <sup>11</sup> L. Šmejkal, J. Sinova and T. Jungwirth, Phys. Rev. X **12**, 031042 (2022).
- <sup>12</sup> I. Mazin Phys. Rev. X **12**, 040002 (2022).
- <sup>13</sup> L. Šmejkal, J. Sinova and T. Jungwirth, Phys. Rev. X **12**, 040501 (2022).
- <sup>14</sup> X. Chen, D. Wang, L. Y. Li and B. Sanyal, Preprint at https://arxiv.org/abs/2104.07390 (2021).
- <sup>15</sup> P. J. Guo, Z. X. Liu and Z. Y. Lu, npj Comput. Mater. 9, 70 (2023).
- <sup>16</sup> S. D. Guo, X. S. Guo, K. Cheng, K. Wang and Y. S. Ang, Preprint at https://doi.org/10.48550/arXiv.2306.04094 (2023).
- <sup>17</sup> H.-Y. Ma, M. L. Hu, N. N. Li, J. P. Liu, W. Yao, J. F. Jia and J. W. Liu, Nat. Commun. **12**, 2846 (2021).
- <sup>18</sup> Y. J. Niu, H. F. Lv, X. J. Wu and J. L. Yang, J. Phys. Chem. Lett. **14**, 4042 (2023).
- P. Hohenberg and W. Kohn, Phys. Rev. **136**, B864 (1964);
   W. Kohn and L. J. Sham, Phys. Rev. **140**, A1133 (1965).
- <sup>20</sup> G. Kresse, J. Non-Cryst. Solids **193**, 222 (1995).
- <sup>21</sup> G. Kresse and J. Furthmüller, Comput. Mater. Sci. 6, 15 (1996).

- <sup>22</sup> G. Kresse and D. Joubert, Phys. Rev. B **59**, 1758 (1999).
- <sup>23</sup> J. P. Perdew, K. Burke and M. Ernzerhof, Phys. Rev. Lett. 77, 3865 (1996).
- $^{24}\,$  Q. L. Sun and N. Kioussis, Phys. Rev. B  $\bf 97,$  094408 (2018).
- <sup>25</sup> C. Ma, X. J. Chen, K. J. Jin et al., J. Phys. Chem. Lett. 14, 825 (2023).
- <sup>26</sup> Q. Y. Ma, W. H. Wan, Y. M. Li and Y. Liu, Appl. Phys. Lett. **120**, 112402 (2022).
- <sup>27</sup> X. Wu, D. Vanderbilt and D. R. Hamann, Phys. Rev. B 72, 035105 (2005).
- <sup>28</sup> A. Togo, F. Oba and I. Tanaka, Phys. Rev. B **78**, 134106 (2008).
- <sup>29</sup> R. C. Andrew, R. E. Mapasha, A. M. Ukpong and N. Chetty, Phys. Rev. B 85, 125428 (2012).
- <sup>30</sup> W. Y. Tong, S. J. Gong, X. Wan, and C. G. Duan, Nat. Commun. 7, 13612 (2016).
- <sup>31</sup> P. Jiang, X. H. Zheng, L. L. Kang, X. X. Tao, H. M. Huang, X. C. Dong and Y. L. Li, J. Mater. Chem. C **11**, 2703 (2023)
- <sup>32</sup> S. D. Guo, J. X. Zhu, M. Y. Yin and B. G. Liu, Phys. Rev. B 105, 104416 (2022).
- <sup>33</sup> S. D. Guo, W. Q. Mu and B. G. Liu, 2D Mater. 9, 035011 (2022).
- <sup>34</sup> S. D. Guo, Y. L. Tao, W. Q. Mu and B. G. Liu, Front. Phys. 18, 33304 (2023).
- <sup>35</sup> S. Li, Q. Q. Wang, C. M. Zhang, P. Guo and S. A. Yang, Phys. Rev. B **104**, 085149 (2021).
- <sup>36</sup> W. Y. Pan, Phys. Rev. B **106**, 125122 (2022).
- <sup>37</sup> L. Dong, J. Lou and V. B. Shenoy, ACS Nano, **11**, 8242 (2017).
- <sup>38</sup> M. N. Blonsky, H. L. Zhuang, A. K. Singh and R. G. Hennig, ACS Nano 9, 9885 (2015).
- <sup>39</sup> K. N. Duerloo, M. T. Ong and E. J. Reed, J. Phys. Chem. Lett. 3, 2871 (2012).
- <sup>40</sup> L. Zhu, Y. Zhang, P. Lin et al., ACS Nano **12**, 1811 (2018).
- <sup>41</sup> R. W. Zhang, C. X. Cui, R. Z. Li, J. Y. Duan, L. Li, Z. M. Yu and Y. G. Yao, Preprint at https://doi.org/10.48550/arXiv.2306.08902 (2023).
- <sup>42</sup> A. O. Fumega and J. L. Lado, Nanoscale **15**, 2181 (2023).